STRUCTURE AND INFRASTRUCTURE ENGINEERING
2023, VOL. 19, NO. 2, 178–196
https://doi.org/10.1080/15732479.2021.1931893

Model updating of seven-storey cross-laminated timber building designed on frequency-response-functions-based modal testing

Blaž Kurent[a], Boštjan Brank[a] and Wai Kei Ao[b]

[a]Faculty of Civil and Geodetic Engineering, University of Ljubljana, Ljubljana, Slovenia; [b]College of Engineering, Mathematics and Physical Sciences, University of Exeter, Exeter, UK

ABSTRACT
Based on the experimental estimation of the key dynamic properties of a seven-storey building made entirely of cross-laminated timber (CLT) panels, the finite element (FE) model updating was performed. The dynamic properties were obtained from an input-output full-scale modal testing of the building in operation. The chosen parameters for the FE model updating allowed the consideration of the timber connections in a smeared sense. This approach led to an excellent match between the first six experimental and numerical modes of vibrations, despite spatial aliasing. Moreover, it allowed, together with the sensitivity analysis, to estimate the stiffness (affected by the connections) of the building structural elements. Thus, the study provides an insight into the as-built stiffness and modal properties of tall CLT building. This is valuable because of the currently limited knowledge about the dynamics of tall timber buildings under service loadings, especially because their design is predominantly governed by the wind-generated vibrations.

ARTICLE HISTORY
Received 16 February 2021
Revised 16 April 2021
Accepted 17 April 2021

KEYWORDS
Tall timber building; cross-laminated timber (CLT); dynamic service loading; forced vibration tests; modal parameters; spatial aliasing; finite element model updating

1. Introduction

An evolution in timber building technologies has enabled construction of tall timber buildings (TTBs) with structural elements made from cross-laminated timber (CLT). An example is the seven-storey Yoker building in Glasgow, UK, see Figure 1, which was the tallest Scottish timber building when constructed in 2017. In general, TTBs have sufficient capacity to resist lateral loads for the ultimate limit state and the design is governed by the wind-generated vibrations that cause discomfort or annoyance to occupants (e.g. Edskär & Lidelöw, 2017; Johansson, et al., 2016; Reynolds, Harris, Chang, Bregulla, & Bawcombe, 2015). The amount of sway/acceleration depends on the mass and stiffness distribution across the TTB and its ability to dissipate kinetic energy (e.g. Malo, Abrahamsen, & Bjertnaes, 2016). Currently, the knowledge on the stiffness and the key dynamic properties (natural frequencies, mode shapes and damping) of TTBs is limited, particularly with respect to connections used (e.g. Abrahamsen et al., 2020), which is one of the main barriers for further TTBs developments. Underestimation of the fundamental natural frequency of up to 50% by a TTB structural model, relative to its experimental counterpart, is common (e.g. Ao & Pavic, 2020).

The modal properties of TTBs are difficult to predict, however it is possible to learn about the as-built modal properties of the operational TTBs. Output-only ambient vibration testing (AVT) was performed for a limited number of tall CLT buildings (see, Aloisio, Pasca, Tomasi, & Fragiacomo, 2020; Mugabo, Barbosa, & Riggio, 2019; Reynolds, Casagrande, & Tomasi, 2016; Reynolds et al., 2015), where the fundamental vibration modes were identified and compared with FE results. The AVT methods are based on measured response due to unmeasured ambient excitation, which varies with time and produces estimates that vary from one data block to another. On the other hand, in the input-output modal testing, both the excitation force and the corresponding dynamic response are measured, which allows to estimate FRFs and use them to get a more reliable estimation of the as-built modal properties (e.g. Ao & Pavic, 2020). In particular, the properties of higher modes of vibration are much easier to measure and investigate using the FRF-based methodology. However, FRFs have been non-existing in the TTBs studies. One reason is practical difficulties related to forced excitation of a TTB without damaging it, which can be overcome by using a refined (best-engineering judgement) FE model before and during the test. The next reason is complication in measuring responses simultaneously throughout the building, which can be solved by using synchronised wireless accelerometers (see, Ao & Pavic, 2020).

With the experimental modal properties at hand, an insight into the distribution of mass and stiffness over the tested TTB can be gained by performing the FE model updating (e.g. Mottershead, Link, & Friswell, 2011). The latter can provide information about the influence of

CONTACT Boštjan Brank bbrank@fgg.uni-lj.si Faculty of Civil and Geodetic Engineering, University of Ljubljana, Jamova c. 2, SI-1000 Ljubljana, Slovenia

(a) Photo from November 2019.

(b) Distribution of CLT panels for external walls.

Figure 1. Yoker, 7-storey CLT building in Glasgow, UK.

connections/joints on the stiffness of TTB's structural components, for example CLT walls and floors. The problem of choosing the updating parameters is a crucial part of the FE model updating and can be assisted with the sensitivity analysis (e.g. Borgonovo & Plischke, 2016; Saltelli et al., 2008). The latter gives an insight how the FE model responds due to a change of a parameter value, and it is a great tool for exploration of a choice for updating parameters. Before the FE model updating is performed, the FE and experimental vibration modes must be correlated. When sensors do not capture enough motion of the structure, the problem of spatial aliasing needs to be overcome (e.g. Fotsch & Ewins, 2001; Yaghoubi & Abrahamsson, 2014).

In this work, the dynamics under service loadings of the tall CLT building from Figure 1 is studied. Our approach is in contrast with the previous studies, which were based on the AVT methods and were using simple FE/analytical models for correlating experimental results with numerical/analytical solutions. It is for the first time that the information about the operational tall CLT building is obtained by the FE model updating that uses a refined FE model and relies on FRF-based vibration tests. The chosen updating parameters enabled inclusion of the effects of the connections/joints in a smeared manner, which led to an excellent match between the experimental and numerical results. In particular, the first six vibration modes are matched almost perfectly after the FE model updating. This is an excellent result in comparison with the only (to our best knowledge) previous study on the model updating of tall CLT building by Aloisio et al. (2020), where the three vibration modes were balanced. We note that matching of the higher-order modes is much more difficult to achieve than matching of the lower modes, because one needs both reliable (FRF-based) vibration tests (Ao & Pavic, 2021) and a prudent choice of updating parameters of a refined FE model. The results of our FE model updating clearly show how the connections impact the stiffness of the CLT walls and CLT floors of the considered building.

At the closure of this section let us recall that the important part of CLT building is steel connections, which are of various types and use screws or nails. The present study is adding to the (currently limited) knowledge of how much the connections contribute to the overall stiffness of a tall CLT building under service loadings. According to Aloisio et al. (2020), Gavric, Fragiacomo, and Ceccotti (2015) and Reynolds et al. (2015), the connections operate far below their strength at low-amplitude movements and the load transfer between the panels occurs mainly through the friction and direct contact, enabling the panels to deform in shear and bending. In joints with small friction (such as those in CLT floors), sliding between the CLT panels might occur for service dynamic loadings. According to the laboratory tests presented by Brandner et al. (2017), D'Arenzo, Casagrande, Reynolds, and Fossetti (2019), Oh et al. (2017) and Yasumura, Kobayashi, Okabe, Miyake, and Matsumoto (2016), the connections influence the in-plane stiffness of CLT floors and walls. Moreover, this stiffness is non-trivially dependent on several other factors, such as panel fabrication, boundary conditions affecting the development of shear mechanism, and the number and orientation of panels in a composition. Studies by Ashtari, Haukaas, and Lam (2014) and D'Arenzo et al. (2019) concluded that the sliding between the panels is the main factor contributing to the in-plane flexibility of CLT floors.

As for the shear walls, Yasumura et al. (2016) tested two two-storey CLT structures against lateral load, where the shear walls of the first and the second structure were composed of large and small panels, respectively, and for the former case, the initial stiffness was approximately twofold of the former. A difference in the initial in-plane shear stiffness was also reported by Oh et al. (2017) for the three walls made of single, two and four panels. As for the value of the in-plane shear modulus for CLT, the study by Brandner et al. (2017) on single CLT panels describes their shear mechanism as either gross-shear or net-shear. According to Brandner et al. (2017), the narrow-face bonded CLT panels with no cracks develop the gross-shear and have approximately 50% higher in-plane shear modulus than the CLT panels with cracks and/or gaps (because the narrow faces are not glued) that develop net-shear. The above-mentioned laboratory results indicate that the FE modelling of CLT walls and floors in TTBs has to deal with a large variance in the in-plane shear modulus value of CLT and uncertainty regarding the influence of connections.

The rest of the paper is organized as follows. In Section 2, the seven-storey CLT building is briefly described, and Section 3 presents the best-engineering-judgement FE model of the building. The experimental results are summarized in Section 4, and the FE model updating is presented in Section 5. The updating of the FE model that includes foundation is discussed in Section 6, and conclusions are drawn in Section 7.

2. Building description

The seven-storey residential building has a T-shape with clearly separated but structurally still connected northern and southern wings, see Figure 1. The structural system of the building is made completely out of CLT panels, apart from the reinforced concrete foundation and ground floor slab, and a few steel beams and frames that locally reinforce the timber. The characteristic dimensions of the building are: 31 m by 28 m in plan, 22 m in height above the ground floor slab, 3745 m^2 gross floor area, and 550 m^2 foot print area. Typical floor plan is shown in Figure 2(a). The facade does not include any secondary load-bearing elements that could contribute to the structural stiffness. The soil layer under the building is made ground. Beneath that is a layer of glacial till, considered as appropriate foundation bearing material for the multi-storey building. The foundation is described in Section 6.

Five different types of CLT panels were used, varying in thickness from 100 mm to 140 mm (except for the stair half-landing with 200 mm CLT panels), having either 3 or 5 layers, see Table 1. As shown in Figure 1(b), the external walls (as well as some internal walls) consist of large CLT panels, with pre-cut openings for windows, which have the height of the storey and the length of the building edge (except for the last storey, where this is not the case). The CLT panels in the Yoker building are typically connected using a combination of angle brackets and wood screws, see Figure 2. The manufacturer Stora Enso, see Stora Enso (2019), provides mean material properties for their CLT panels (made of C24 spruce boards), see Table 2, which also includes the mean material properties provided by EN-338 for C24 spruce boards.

3. Initial finite element model

This section describes the initial (i.e. the best-engineering-judgement) FE model that is based on the following assumptions: (i) the foundation is rigid and fixed, (ii) the connections do not need to be modelled, and (iii) the floors are flexible (i.e. the assumption of the rigid-diaphragm is not used). The model was prepared before the tests were performed and proved very helpful for test design.

3.1. Modelling with shell finite elements

Ansys® (2020) software is applied for the construction of the FE model. Figure 3 shows the FE mesh. The CLT panels are modelled by a multi-layer, four-node, shell element with six degrees of freedom per node (called SHELL181). Each layer applies the orthotropic material model with six independent constants (e.g. Brank & Carrera, 2000), for which we adopt material properties provided by the CLT manufacturer Stora Enso, see Table 2. The mean values are taken for stiffness and density, which seems a reasonable choice for undamaged timber. Poisson's ratio ν_{12} is assumed as 0.3 (we note that various values for ν_{12} are reported (see Nairn, 2017; Rocco Lahr et al., 2015; Stürzenbecher, Hofstetter, & Eberhardsteiner, 2010)). The mid-surfaces of the shell finite elements are placed in accordance with the positions of the mid-planes of the CLT panels, as shown in Figure 4(b). The connections between CLT panels are not explicitly modelled and a perfect bond is assumed. In the bottom horizontal plane of the FE mesh, which is at the level of the top surface of the reinforced concrete ground floor, all degrees of freedom are set to zero.

3.2. Modelling the building stiffness and mass

Structural elements that are modelled as entities with stiffness are: the external and internal load-bearing walls, floors, roof, and elevator shaft. We neglect the steel beams and frames that locally reinforce the timber (they add up to less than 1% of the total mass of the load-bearing structure). We also neglect the building elements that are traditionally considered negligible for the overall building stiffness, e.g. non-load-bearing partition walls (these partition walls account for about 6% of the total mass of the walls in a storey), stairs, windows, etc.

The mass of the well-documented non-structural building elements (i.e. facade, insulation, screed, flooring, fireline board, cladding, and non-load-bearing partition walls) is taken into account as uniformly distributed area mass over walls and floors. The sum of masses of non-structural elements attached to the walls of a particular storey is smeared over the FEs that model the walls in that storey. The sum of masses of non-structural elements attached to a particular floor is smeared over the FEs that model that floor. The mass of all undocumented building elements with uncertain weights (such as windows, doors and steel stairs), documented but unevenly distributed elements (various steel reinforcements) and uncertain live load (such as furniture, residents, etc.) are combined into one parameter - uncertain mass - that is estimated to $q = 25\ \mathrm{kg/m^2}$. It is distributed over the FEs that model the floors (it is not distributed over the ground floor and the roof), in particular over the apartment areas (it is not distributed over the corridors). The estimated mass of the building (excluding reinforced concrete foundation and ground floor) is 1270t and can be assigned to the following contributions: around 515t to the timber part of the building, around 685t to the well-documented non-structural elements and around 70t to uncertain mass.

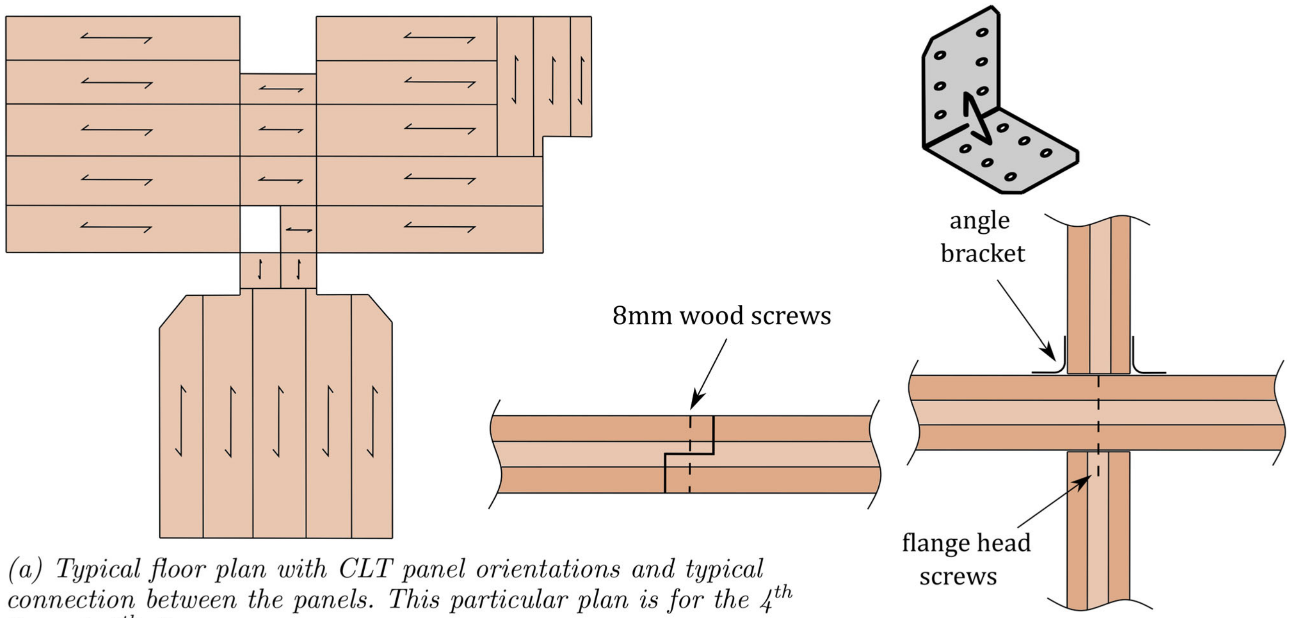

(a) Typical floor plan with CLT panel orientations and typical connection between the panels. This particular plan is for the 4^{th} through 6^{th} floors.

(b) Typical wall-floor joint.

Figure 2. Some details of the Yoker building.

Table 1. Types of CLT panels used.

CLT panel type	Thickness [mm]	Area [m^2]	
		Walls	Floor/roof
SE-100-L3s/SE-100-C3s	100	1149	525
SE-100-L5s/SE-100-C5s	100	968	/
SE-120-L3s/SE-120-C3s	120	299	/
SE-120-L5s/SE-120-C5s	140	1909	2926
SE-140-L5s/SE-140-C5s	140	1109	190
SE-200-L5s	200	/	49

Table 2. Mean material properties for CLT.

Property	Stora Enso	EN 338
Elastic modulus E_1 [MPa]	12 000	11 000
Elastic modulus $E_2 = E_3$ [MPa]	by EN 338	370
Shear modulus $G_{12} = G_{13}$ [MPa]	460	690
Shear modulus G_{23} [MPa]	50	/
Density ρ [kg/m^3]	470	420

3.3. Convergence analysis

The convergence analysis was performed in order to find an optimal mesh. To that end, the natural frequencies were computed by modal analysis for nine different FE meshes. The results are shown in Figure 5, where the convergence is presented for the first six natural frequencies in terms of the relative difference $\Delta_i(\mathcal{M})$. The latter is defined for the i-th natural frequency f_i and mesh $\mathcal{M}$ as:

$$\Delta_i(\mathcal{M}) = \frac{f_i(\mathcal{M}) - f_i(\mathcal{M}_f)}{f_i(\mathcal{M}_f)} \tag{1}$$

where $\mathcal{M}_f$ denotes the finest mesh with 2.79×10^6 nodes. Figure 5 shows that finer meshes lower natural frequencies. For the subsequent work, we choose mesh $\mathcal{M}_a$ with 2.61×10^5 nodes, as a trade-off between accuracy and computational time. By assuming that the finest mesh $\mathcal{M}_f$ yields converged results, the approximate discretization error

$$\Delta_i(\mathcal{M}_a) = \frac{f_i(\mathcal{M}_a) - f_i(\mathcal{M}_f)}{f_i(\mathcal{M}_f)} \tag{2}$$

can be computed for the applied mesh $\mathcal{M}_a$. The following numbers are obtained for the first six natural frequencies: 1.10%, 0.82%, 1.14%, 1.29%, 0.87%, 0.69%.

3.4. Natural frequencies and mode shapes

Table 3 presents the first six mode shapes and the related natural frequencies. We adopt the ordering based on the correlation with the experimental modes shown below in Section 4.2 and Table 4. The first three modes are very closely spaced in terms of frequencies. The 1^{st} mode is bending mode in the weaker building direction. Modes 2 and 3 are torsion (almost a mirroring) modes. Mode 4 is a more complex torsion mode with opposite rotations of the two building parts (hereinafter denoted as the" web" and the" flange" of the T-shaped building). Mode 5 is a shear mode showing, along with modes 4 and 6, in-plane deformations of floor slabs. Mode 6 is a higher-order bending mode.

4. Experimental results

This section provides a brief description of the FRF-based modal testing of the Yoker building in operation. In addition, the experimental results are compared with the results of the initial FE model.

4.1. FRF-based modal testing

Three synchronised APS Model 400 electrodynamic shakers with total moving mass of 68.85 kg were installed on the 6^{th}

Table 3. First six FE mode shapes and respective deformations of the 6th floor (the experimental mode order is adopted).

Mode	Frequency	Mode shape	6th floor deformation
1	2.85 Hz	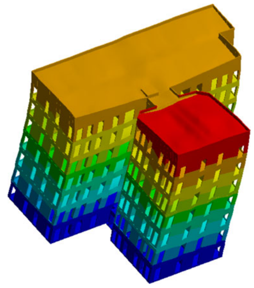	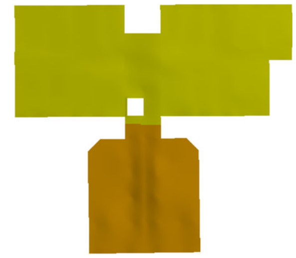
2	2.81 Hz	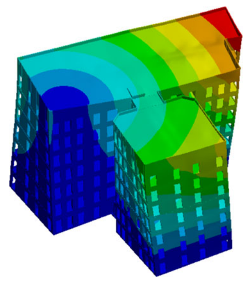	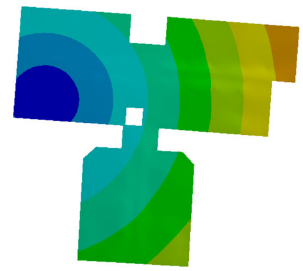
3	2.94 Hz	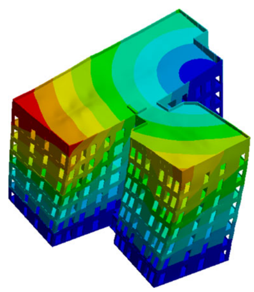	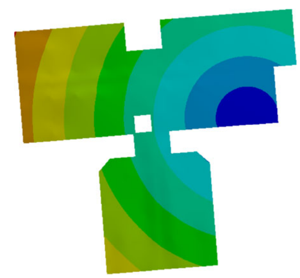
4	3.98 Hz	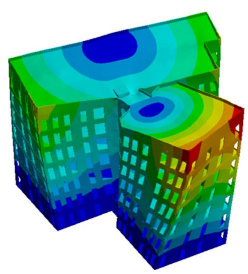	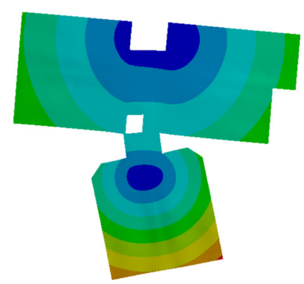
5	8.32 Hz	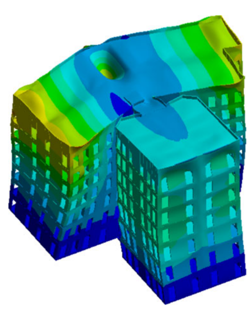	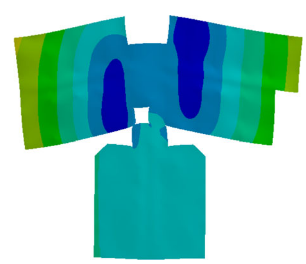
6	8.19 Hz	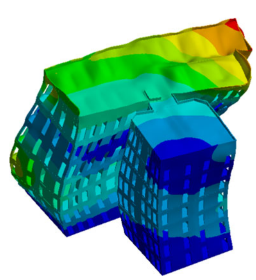	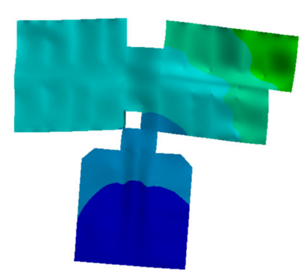

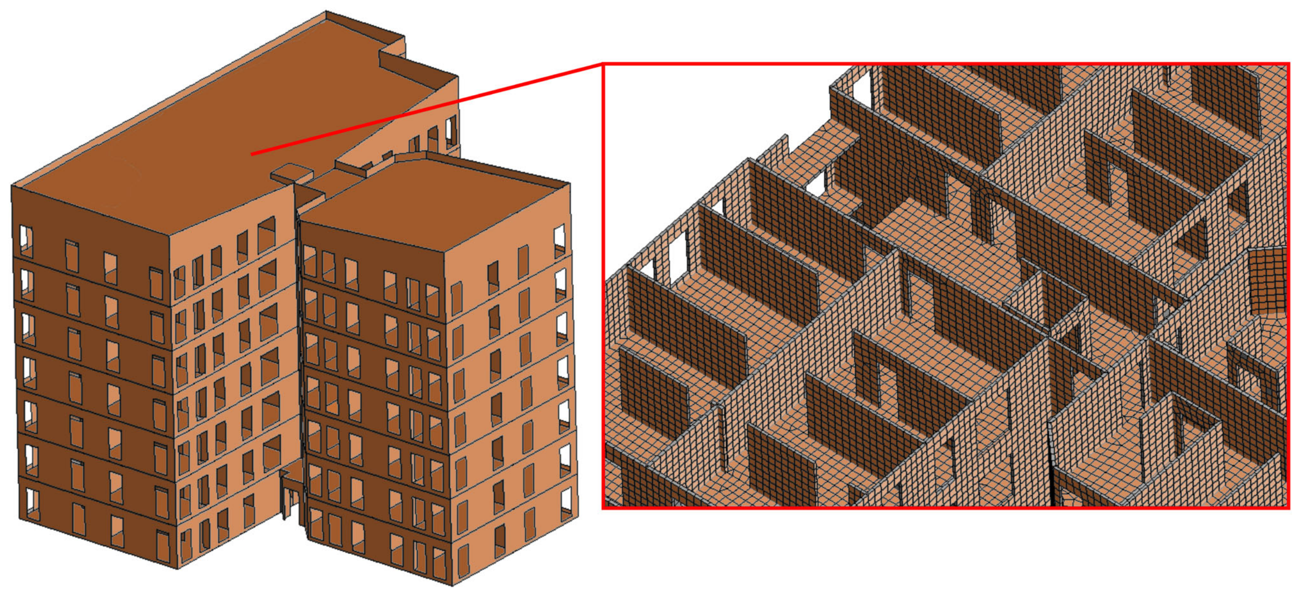

Figure 3. Model geometry (left) and detail of the FE mesh (right).

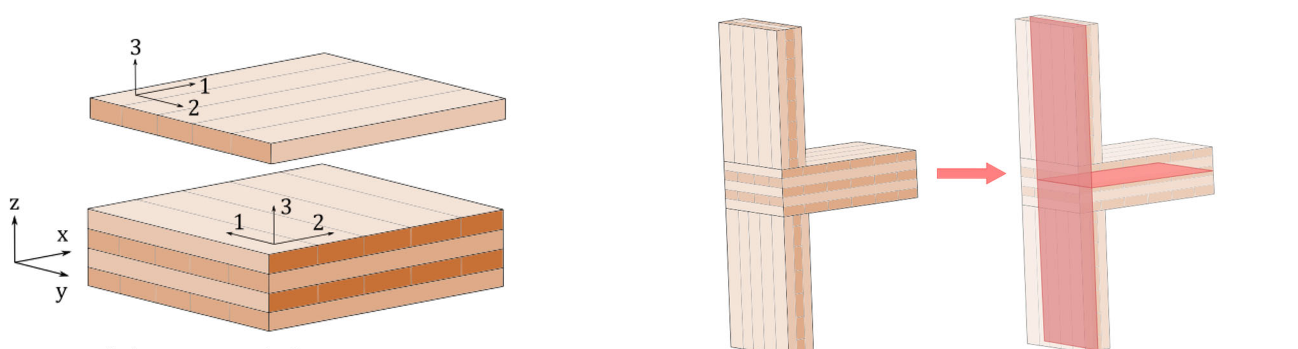

(a) Layers of CLT panel.

(b) CLT panels and mid-surfaces of shell elements.

Figure 4. CLT panel (left) and modelling detail (right).

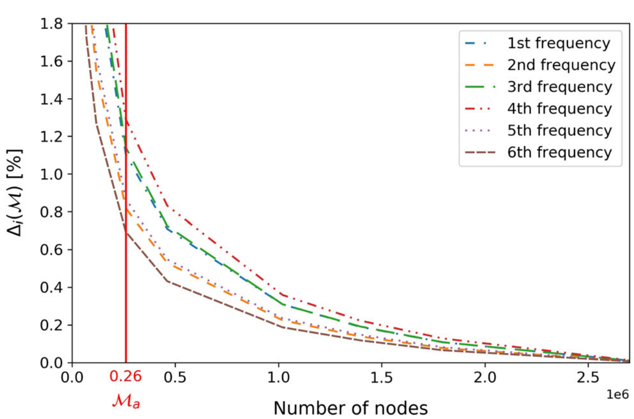

Figure 5. Convergence analysis results.

floor, see Figure 6. Honeywell QA750 and Japan Aviation Electronics Industry, Limited JA-70SA accelerometers were used to measure accelerations. Altogether 13 sensor locations were chosen with 2 sensor locations on each floor (no sensors were placed on the ground floor) and additional one on the 6th floor as a reference sensor near the shakers. Each sensor location measured acceleration in two horizontal directions, as shown in Figure 7. At the time of the measurements, the building was operational so installation of the sensors was limited to the corridors in the core of the building. Since the measured degrees of freedom do not give sufficient information about the motion of the whole building (see modes 4 to 5 in Table 3), some degree of spatial aliasing is expected.

Table 4. Comparison of initial FE model and experimental results.

Experiment		Initial FE model		
i	Frequency	j	Frequency	MAC$_i$
1	2.85 Hz	2	2.85 Hz	0.77
2	2.93 Hz	1	2.81 Hz	0.77
3	3.13 Hz	3	2.94 Hz	0.38
4	3.63 Hz	4	3.98 Hz	0.95
5	6.73 Hz	6	8.32 Hz	0.80
6	8.74 Hz	5	8.19 Hz	0.78
7	9.68 Hz	11	9.39 Hz	0.66
8	11.9 Hz	58	15.3 Hz	0.72

Two sets of random excitation vibration tests were carried out, one with shakers exciting in the x direction and the other in the y direction (see Figure 7 for the directions). The average amplitude of the total force was around 500 N and the location near the shaker had the average structural responses of 0.005 m/s^2 and 0.004 m/s^2 in the x and y directions, respectively. The excitation signal was wide frequency bandwidth white noise (0 Hz–10 Hz). Single-input multiple-output modal identification method (complex mode indicator function) was used to identify 8 vibration modes. Typical FRFs of the test point near the electrodynamic shakers presented in Figure 8 show that the lowest natural frequencies were clustered. The measured natural frequencies are presented in Table 4 and compared with the FE results. The experimental mode shapes and the corresponding mode shapes obtained with the initial FE model are shown below in Table 8.

Figure 6. Test equipment in the 6th floor.

4.2. Comparison of experimental and numerical results

Modal assurance criterion (MAC) is a commonly used measure for the correlation between two sets of modes (e.g. Allemang, 2003), computed as:

$$\mathrm{MAC}(\boldsymbol{\psi}_{i,e}, \boldsymbol{\psi}_{j,n}) = \frac{\left|\boldsymbol{\psi}_{i,e}^{T}\boldsymbol{\psi}_{j,n}^{*}\right|^{2}}{\left(\boldsymbol{\psi}_{i,e}^{T}\boldsymbol{\psi}_{i,e}^{*}\right)\left(\boldsymbol{\psi}_{j,n}^{T}\boldsymbol{\psi}_{j,n}^{*}\right)}, \tag{3}$$

where $\boldsymbol{\psi}_{i,e}$ and $\boldsymbol{\psi}_{j,n}$ are i-th experimental and j-th numerical mode shapes, respectively, and $*$ denotes the conjugation of complex mode shapes. MAC value 1 suggests a strong similarity between two modes, whereas value 0 suggests no similarity. Commonly, all experimental and numerical mode shapes are compared pair-by-pair and presented in MAC matrix, which is ideally a diagonal unit matrix. Figure 9

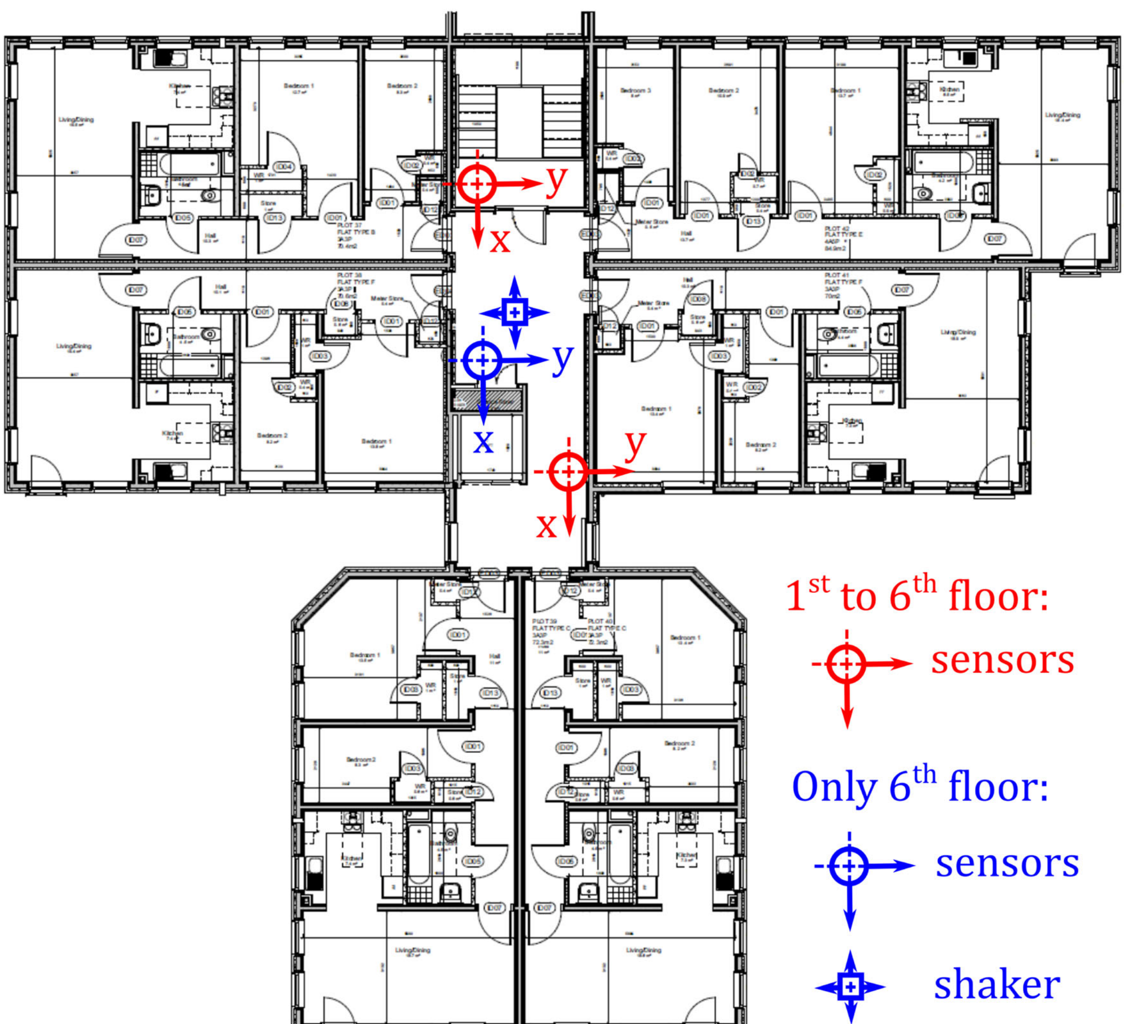

Figure 7. Layout of shakers and sensors.

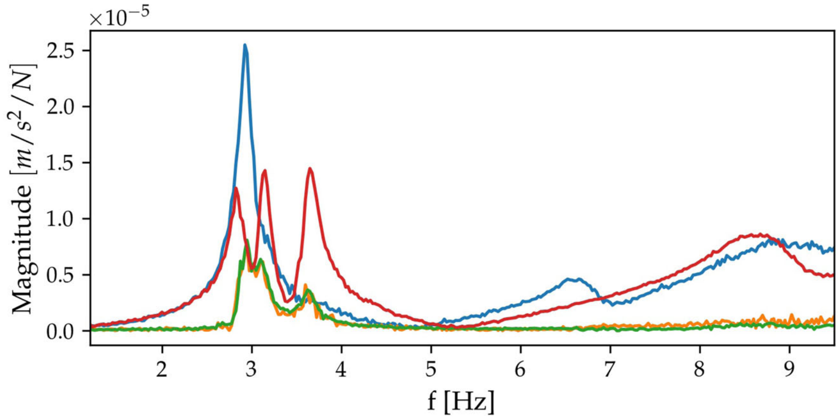

Figure 8. Typical FRFs.

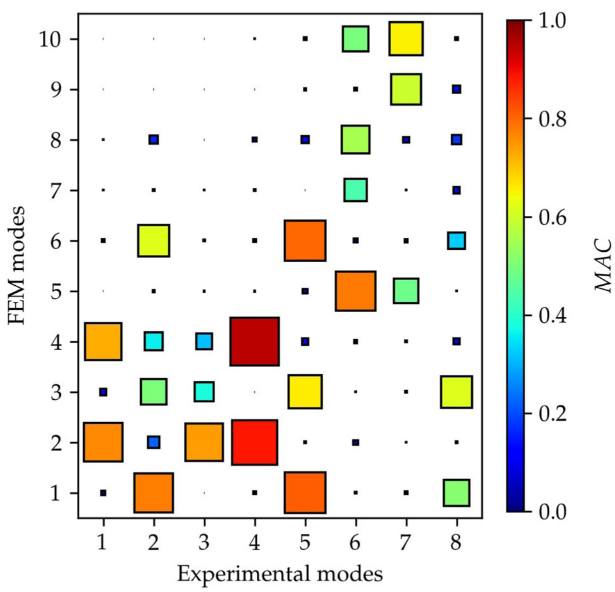

Figure 9. MAC matrix for the initial FE model.

shows that MAC matrix is far from diagonal and there are quite a few correlated mode shapes. This is a consequence of spatial aliasing, which can occur not only when too few sensors are used but also when they are placed so that not enough features of the mode shapes are captured (e.g. Allemang, 2003; Liu, Yan, & Guedes Soares, 2018; Yaghoubi & Abrahamsson, 2014). In our case, poor sensor placement can be suspected already from the layout presented in Figure 7. Spatial aliasing can also be confirmed by examining the Auto-MAC matrices (see Ewins, 2000) in Figure 10, which display many non-zero off-diagonal terms. However, the spatial aliasing was inevitable due to limited access to the building.

With spatial aliasing, additional information is needed to find matching pairs of modes. Sometimes, a criterion that combines the MAC value and the frequency is used (e.g. Petersen & Øiseth, 2017), but in our case, the frequencies in question are so close that such a criterion does not separate between a good and a bad mode pair. We used the Auto-MAC matrices in order to find matching mode pairs. First, the MAC matrix was compared with the experimental Auto-MAC matrix, shown in Figure 10(a). It can be seen that the 1st row of the experimental Auto-MAC matrix strongly resembles the 2nd row of the MAC matrix, but it is also very similar to the 4th row of the MAC matrix. Comparing also the frequencies of those modes, it can be concluded that the 1st experimental mode matches the 2nd FE mode. In a similar fashion, we connected the 2nd experimental to the 1st FE mode, the 4th experimental to the 4th FE mode, the 5th experimental to the 6th FE mode, and the 6th experimental to the 5th FE mode. This leaves us with the only reasonable connection left between the 3rd experimental and the 3rd FE mode. The pairs can also be confirmed by comparing the columns of the FE Auto-MAC matrix in Figure 10(b) with the columns of the MAC matrix.

How well (in terms of natural frequencies and MAC_i values) the modes match is shown in Figure 11 using the plot of frequency scaled modal assurance criterion (FMAC) introduced by Fotsch and Ewins (2000, 2001). MAC_i is defined as the MAC value of i^{th} matching pair, $i = 1, \ldots, 8$ (the order coincides with the order of experimental modes), and the relative error of the numerical frequency is defined as

$$\frac{f_{i,\,\exp} - f_{i,\,FEM}}{f_{i,\,\exp}}. \tag{4}$$

Let us note that although some MAC values in Table 4 are not sufficiently high and the frequency differences are too large for a clear pairing of modes, we match them for the purpose of model updating and later comparison.

5. Model updating

In this section, we explain the choice of parameters for the FE model updating and interpret the results of sensitivity analysis and model updating.

5.1. Parameter selection

After the initial screening sensitivity analysis, we can conclude that the following parameters are important: elastic modulus E_1, in-plane shear modulus G_{12}, timber density ρ, and uncertain mass q. These parameters significantly affect the natural frequencies and mode shapes. We could also conclude that elastic modulus E_2, out-of-plane shear moduli (G_{13} and G_{23}), and Poisson's ratio ν_{12} have little influence on the results. Moreover, timber density has a similar effect as uncertain mass q. On this basis, six parameters from Table 5 are chosen for more detailed sensitivity analysis and FE model updating. From Table 5 it can be seen that there are three and two parameters associated with major elastic modulus and in-plane shear modulus, respectively. This way, we want to accommodate for the effects of connections in a smeared sense. We know in advance that after the updating most of the parameters from Table 5 will not represent the material properties because they will be" polluted" with the modelling error. The chosen ranges of the parameters reflect not only the information on the material data, see Table 2, but also allow capturing the stiffness reduction of walls and floors due to the connections. The range for mass parameter accommodates for uncertain weights of structural and non-structural building elements and live loads.

5.2. Shear wall stiffness reduction due to the wall-floor joint

The wall-floor joint shown in Figure 2(b) reduces the stiffness of the shear wall. The initial FE model does not consider this reduction, because it models the wall-floor joint as shown in Figure 4(b). We expect that the parameter e_1 will take this effect into account in a smeared sense. The effect of the wall-floor joint on the vertical axial stiffness of the shear wall can be explained as shown in Figure 12. For illustration purposes only, we assume that a unit depth of one storey of the shear wall, consisting of vertical and horizontal CLT panels denoted as A and B, respectively, is supported at the bottom and imposed to unit axial displacement at the top. It is discretized with either (i) two bar FEs with elastic moduli $E_0 = E_1$ and $E_{90} = E_2$ for elements A and B, or (ii) one bar FE with effective elastic modulus μE_0. Equating the forces that produce unit displacement gives the value for μ. Figure 13 shows μ as a function of γ, which takes into account the effective width of the floor CLT, and as a function of α for different configurations of CLT panels from Table 1 used for the walls, $\alpha \in [0.6, 0.7]$. It can be seen that this simple analysis gives $\mu \in (\approx 0.5, \approx 0.7)$ for $\gamma \in [1, 2]$.

5.3. In-plane stiffness of CLT walls and floors

On each storey, the shear walls of the Yoker building are composed of large CLT panels with pre-cut openings, the lengths of which equal the lengths of the building edges, see Figure 1. These panels, which are constrained on their top and bottom with CLT floors, are under axial compression (due to gravity) producing large friction in the wall-floor joints. On the other hand, the floors are composed of a number of CLT panels, as can be observed from Figure 2(a), with small friction between the panels. Furthermore, the" web" and the" flange" of the building are connected only by a narrow strip, which defines the specific geometry of the CLT floors and influences their in-plane behaviour. These differences in geometry and panel layouts suggest that the in-plane shear stiffness for the CLT shear walls and CLT floors may differ considerably. To account for this, the parameters g_1 and g_2 were introduced. Moreover, another parameter, e_3, was introduced to capture the effect of the floor connections in a smeared sense (besides g_2).

5.4. Sensitivity analysis

Sensitivity analysis was performed in order to analyse the influence of the parameters from Table 5 on natural frequencies and MAC values. Variance-based sensitivity analysis was carried out by computing first-order and total effect sensitivity indices. This method is sometimes referred to as Sobol' method or Sobol' variance decomposition (e.g. Borgonovo & Plischke, 2016; Saltelli et al., 2008). The first-order sensitivity index tells us what fraction of total variance $V(Y)$ of response Y can be attributed to parameter X_i. It is computed through the expected value $E_{\sim X_i}(Y|X_i = x_i^*)$ of response Y over all parameters except X_i at fixed value $X_i = x_i^*$. Large variance of this expected value $V_{X_i}(E_{\sim X_i}(Y|X_i))$ over the parameter space of X_i implies a high influence of parameter X_i on response Y. The first-order sensitivity index is computed as a ratio between conditional and total variance:

$$S_i = \frac{V_{X_i}(E_{\sim X_i}(Y|X_i))}{V(Y)}. \tag{5}$$

Another measure of importance is the total effect term. This includes all higher-order terms that also capture interactions between the parameters. The total effect sensitivity index S_{Ti} is defined as:

$$S_{Ti} = 1 - \frac{V_{\sim X_i}(E_{X_i}(Y|X_{\sim X_i}))}{V(Y)}. \tag{6}$$

The expected value of response Y over parameter X_i was computed by fixing all but parameter X_i and finding its variance over all parameters except X_i. If the values of S_i and S_{Ti} are close to zero, parameter X_i does not have much influence on response Y. The higher the values of S_i and S_{Ti} the greater the influence of parameter X_i on response Y. If the values of S_i and S_{Ti} are similar, there is little interaction of parameter X_i with other parameters. Also, if the sum of all terms S_i is equal to 1, the model is said to be additive and there is little interaction between the parameters.

The total number of runs of the FE model in this method is defined as $N(k+2)$, where N is called base sample (usually chosen around 500-1000) and k is the number of parameters. $N = 500$ was chosen, which for $k = 6$ results in 4000 total runs of the FE model. Open source python library SAlib (Herman & Usher, 2017) was used to carry out the sensitivity analysis. Results are presented in Figure 14. Comparing the sensitivity plots from Figure 14(a) and (c), it can be concluded that the parameters influence the first six natural frequencies fairly independently. Indeed, indices S_{Ti} are very close to S_i. Parameter g_1 has a strong influence on all but the 5th natural frequency. On the other hand, g_2 strongly influences the 5th, but has a negligible

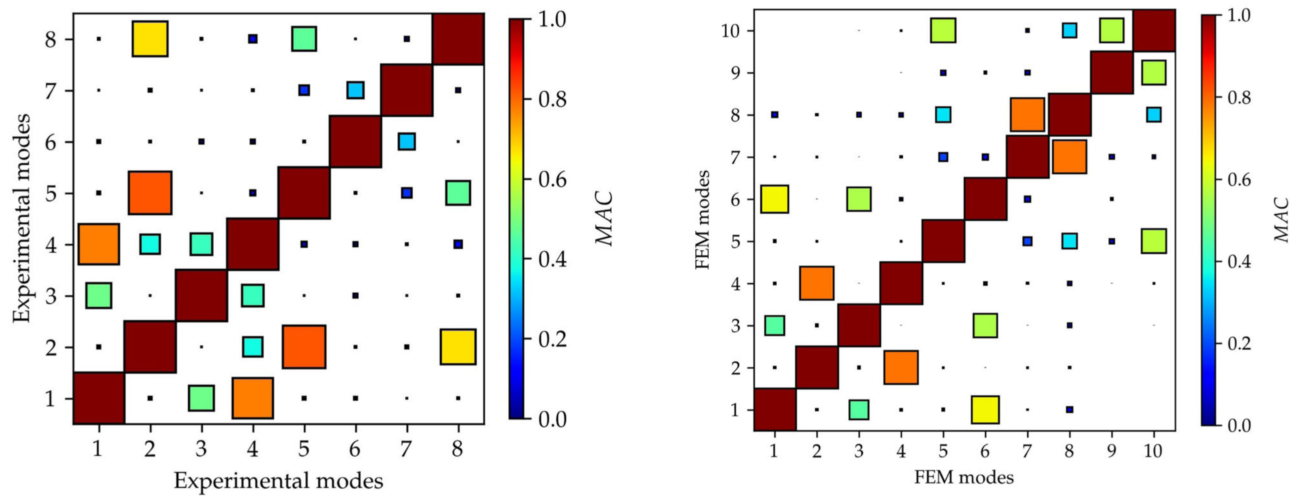

(a) For experimental mode shapes.

(b) For numerical mode shapes.

Figure 10. Auto-MAC matrices.

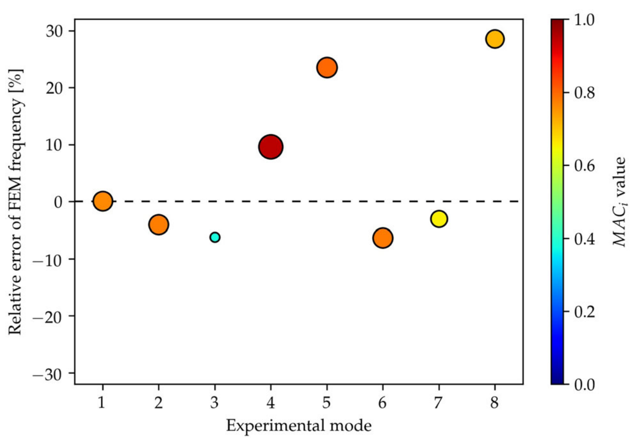

Figure 11. FMAC plot for the initial FE model.

effect on the first three frequencies. Parameter e_1 effects the first natural frequency. It has also a minor impact on the other frequencies, except on the 5th. Parameter e_2 has a negligible effect on all natural frequencies. The same can be said for parameter e_3 for the first three frequencies, while e_3 has a small impact on the last three frequencies. Lastly, q has a moderate effect on all natural frequencies. There is high interaction between the parameters in the effect on MAC_i values. Figure 14(b) and (d) show that the total-effect indices S_{Ti} are much higher than the first-order indices S_i. This means that the effect of one parameter on the response will depend on the values of other parameters.

5.5. Model updating

Two measures of the difference between the computed and measured response were applied. One relates to the similarity of the mode shapes:

$$\delta_{MAC} = \sum_{i=1}^{6} (1 - MAC_i)^2, \tag{7}$$

and the other relates to the difference in natural frequencies:

$$\delta_{freq} = \sum_{i=1}^{6} \left(\frac{f_{i,\,\exp} - f_{i,FEM}}{f_{i,\,\exp}} \right)^2, \tag{8}$$

where $f_{i,\,\exp}$ and $f_{i,FEM}$ are the experimental and numerical natural frequencies of the i-th matching mode pair, respectively. As can be noticed from (7) and (8), only the first six correlated vibration modes are used in the objective functions. Modes 7 and 8 are not considered. Instead, it will be checked after the updating how much they are improved (or worsened) without taking part in the process of updating.

The optimization was performed by using optimization tools incorporated in Ansys, in particular, the multi-objective genetic algorithm with 200 initial samples, 15 maximum iterations, and with 100 samples per iteration. The maximum allowable Pareto percentage is set at 70%, and the convergence stability percentage is set at 1%. The measures (7) and (8) were used as two equally important minimization objective functions. The algorithm converged in 11 iterations, with 1% Pareto percentage and 0.59% stability percentage, giving three candidate points (CP) shown in Table 6. They give us fairly close parameter values (within 3.3% range) so the choice for further observation is somewhat arbitrary. We advance with CP1 as it gives the lowest δ_{freq} and δ_{MAC}.

The results of the FE model updating are shown in Tables 7 and 8, together with the results of the initial FE model and experimental data. The results are also presented with FMAC plot in Figure 15, which can be compared to the FMAC plot of the initial model in Figure 11. It is apparent that all six modes that are included in the objective function have improved compared to the initial model. The most significant improvement is for the mode shape of the 3rd mode and the natural frequencies of the 4th and the 5th modes. The remaining two modes that are not included in the objective function (i.e. 7th and 8th mode) are shown

Table 5. Parameters used in sensitivity analysis and model updating.

Parameter	Range	Property	Application
e_1	6 to 12 GPa	E_1	Used for CLT panels in walls. Only for layers with fibres in vertical direction.
e_2	10 to 13 GPa	E_1	Used for CLT panels in walls. Only for layers with fibres in horizontal direction.
e_3	6 to 12 GPa	E_1	Used for CLT panels in floor slabs. All layers.
g_1	400 to 750 MPa	G_{12}	Used for CLT panels in walls. All layers.
g_2	200 to 500 MPa	G_{12}	Used for CLT panels in floor slabs. All layers.
q	5 to 100 kg m^{-2}	Mass	Additional distributed mass over all the floors.

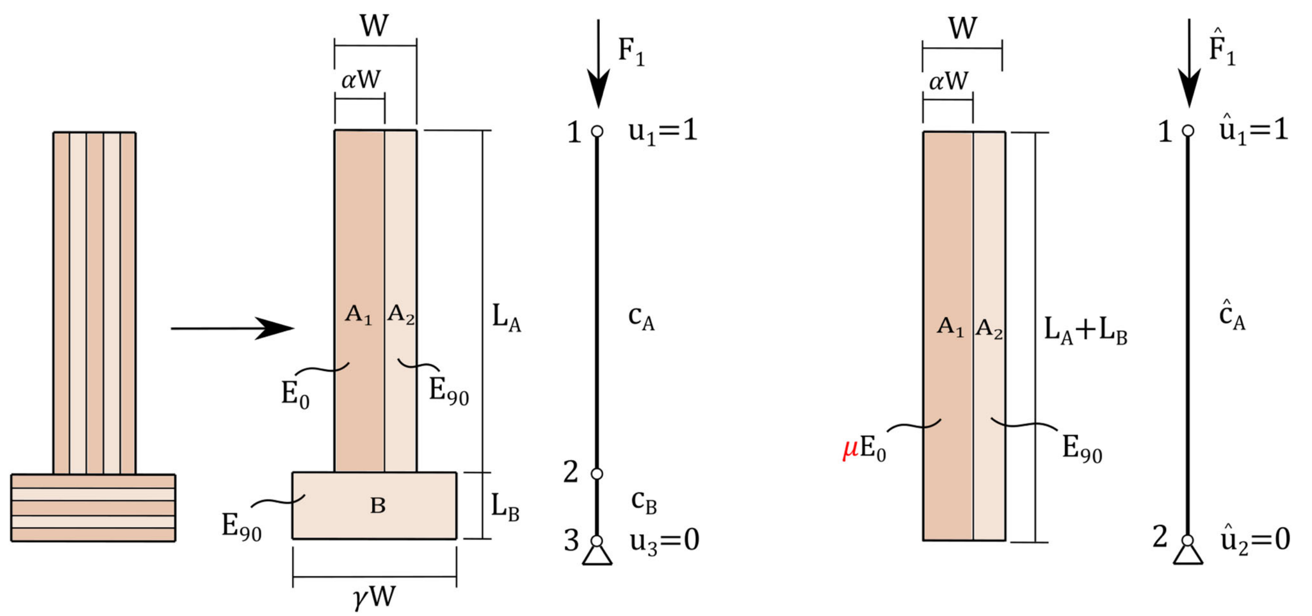

$$c_A = \frac{E_0 \alpha W}{L_A} + \frac{E_{90}(1-\alpha)W}{L_A}$$

$$c_B = \frac{E_{90}\,\gamma\,W}{L_B}$$

$$\begin{Bmatrix} F_1 \\ F_2 = 0 \\ F_3 \end{Bmatrix} = \begin{bmatrix} c_A & -c_A & 0 \\ -c_A & c_A + c_B & -c_B \\ 0 & -c_B & c_B \end{bmatrix} \begin{Bmatrix} u_1 = 1 \\ u_2 \\ u_3 = 0 \end{Bmatrix}$$

$$\hat{c} = \frac{\mu\, E_0\, \alpha\, W}{L_A + L_B} + \frac{E_{90}\,(1-\alpha)\,W}{L_A + L_B}$$

$$\begin{Bmatrix} \hat{F}_1 \\ \hat{F}_2 \end{Bmatrix} = \begin{bmatrix} \hat{c} & -\hat{c} \\ -\hat{c} & \hat{c} \end{bmatrix} \begin{Bmatrix} \hat{u}_1 = 1 \\ \hat{u}_2 = 0 \end{Bmatrix}$$

$$F_1 = \hat{F}_1 \implies \mu = \mu(\alpha, \gamma)$$

Figure 12. Effective axial vertical stiffness of the shear wall due to the wall-floor joint (note that $E_0 = E_1$ and $E_{90} = E_2$).

here as a simple validation that the solution of model updating is reasonable and not overfitting the results. It is also worth noting that the differences in natural frequencies are comparable to the discretization error estimated in Section 3.3. From the MAC matrix in Figure 16, one can see that the updating also improved the order of the numerical modes. By excluding the 6th to 9th numerical modes of the new MAC matrix (with emphasized local deformations), it has a strong resemblance to experimental Auto-MAC matrix from Figure 10(a), even in non-diagonal terms, which is a supporting indication that the problem of spatial aliasing was successfully tackled.

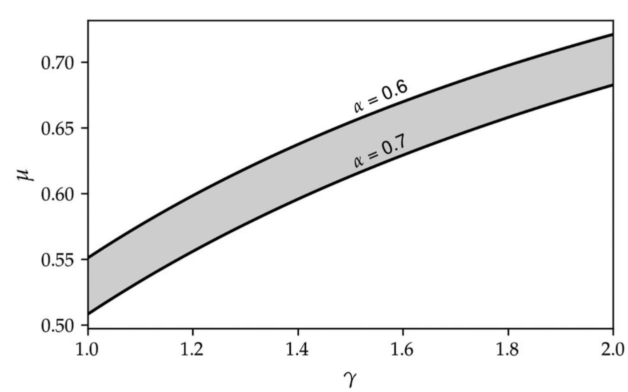

Figure 13. Domain of values for factor μ from Figure 12.

5.6. Updated values of parameters

Parameter e_1 is updated to 50.9% of the initial value. As expected, e_1 captures the effect of the wall-floor joint explained in Section 5.2. With this in mind, the updated value for e_1 seems a reasonable solution. Parameter e_2 is 4.6% higher than what the CLT manufacturer claims for E_1 and the difference can be attributed to the uncertainty of this material property. Let us note, however, that the sensitivity analysis (see Figure 14) showed that the frequencies and MAC_i values are almost unaffected by the change of the

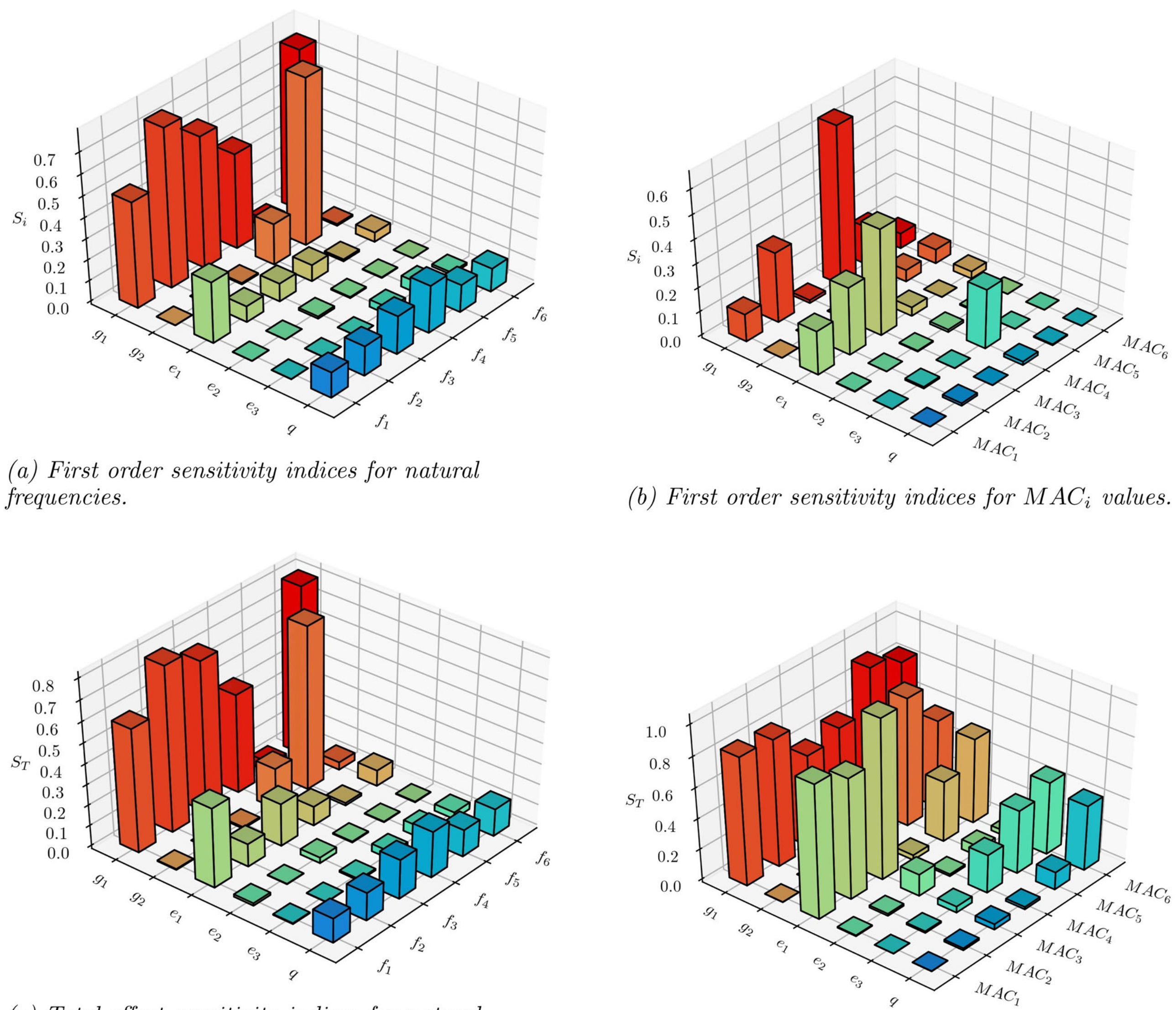

(a) First order sensitivity indices for natural frequencies.

(b) First order sensitivity indices for MAC_i values.

(c) Total effect sensitivity indices for natural frequencies.

(d) Total effect sensitivity indices for MAC_i values.

Figure 14. First order and total sensitivity indices.

value for e_2 (thus the updated result for e_2 may not be very trustworthy). Parameter e_3 is 26.2% lower than the initial value, because it captures the in-plane flexibility of the floors due to connections discussed in Sections 5.3 and 1. Parameter g_2 captures even more the in-plane flexibility of the floors because it settles at 47.6% of the initial value. It is worth recalling that g_2 significantly affects the 5th mode, as well as the 4th and the 6th modes, but it affects negligibly the first three modes, see Figure 14. In other words, the first three modes are almost unaffected by the change of the value for g_2. Large in-plane flexibility of the floors for higher modes may also be partly attributed to the specific floor plan of the Yoker building (see Figures 2 and 7).

A large 61.7% discrepancy between the increased updated value and the initial value can be seen for g_1. In this context, let us note that the uncertainty in the material parameter G_{12} is large, see Table 2 and research by Brandner, Flatscher, Ringhofer, Schickhofer, and Thiel (2016) and Shahnewaz, Tannert, Alam, and Popovski (2017). With this in mind, one can notice that the updated value for g_1 is only 7.8% higher than the value given for G_{12} in EN-338, and 14.5% higher than $G_{12} = 650MPa$ reported by (Brandner et al., 2016) for CLT with narrow face bonding (this is the type of CLT produced by Stora Enso). The above suggests that the updated result for g_1 may be attributed to a large extent to the stochastic nature of G_{12}, and partly to capturing the neglected contributions to the in-plane shear stiffness of the shear walls in the Yoker building. The change of the uncertain mass parameter q contributes to 2.59% increase of the estimated initial mass of the building, which was 1270t. It can be concluded that the updated values for the parameters from Table 6, except the one for e_2, include the effects of the modelling error. Thus, the updated values for e_1, e_3, g_1 and g_2 are not material properties. The modelling error is most pronounced for e_1 (due to the wall-floor joints) and for g_2 (due to the large in-plane flexibility of the floors that may be attributed to the connections and specific floor plan). Large in-plane flexibility of the floors is

Table 6. Values of parameters and objective functions for initial model and for three candidate points representing updated model.

Parameter	Initial model	CP1		CP2		CP3	
		Value	% of initial	Value	% of initial	Value	% of initial
e_1 [GPa]	12	6.11	50.9%	6.23	51.9%	6.24	52.0%
e_2 [GPa]	12	12.55	104.6%	12.45	103.8%	12.57	104.8%
e_3 [GPa]	12	8.85	73.8%	8.98	74.8%	8.98	74.8%
g_1 [MPa]	460	744.1	161.7%	748.0	162.6%	747.8	162.6%
g_2 [MPa]	460	219.0	47.6%	216.1	47.0%	212.0	46.1%
q [kg m^{-2}]	25	36.63	+2.59%[1]	36.88	+2.64%[1]	36.37	+2.53%[1]
δ_{freq} [$\times 10^{-3}$]	74.9	1.87		1.90		1.92	
δ_{MAC} [$\times 10^{-2}$]	58.1	4.53		4.83		4.87	

[1]Difference from initial model presented as a percentage of estimated initial mass of the building.

Table 7. Comparison of initial and updated model with experimental data.

Experiments	Initial model			Updated model		
Frequency	Frequency	Deviation	MAC_i	Frequency	Deviation	MAC_i
2.85 Hz	2.85 Hz	0.11%	0.77	2.84 Hz	−0.41%	0.83
2.93 Hz	2.81 Hz	−4.10%	0.77	2.95 Hz	0.72%	0.99
3.13 Hz	2.94 Hz	−6.07%	0.38	3.08 Hz	−1.54%	0.97
3.63 Hz	3.98 Hz	9.64%	0.95	3.77 Hz	3.75%	0.96
6.73 Hz	8.32 Hz	23.6%	0.80	6.70 Hz	−0.46%	0.95
8.74 Hz	8.19 Hz	−6.64%	0.78	8.64 Hz	−1.16%	0.90
9.68 Hz	9.39 Hz	−3.05%	0.66	9.38 Hz	−3.11%	0.78
11.9 Hz	15.3 Hz	28.6%	0.72	12.4 Hz	4.30%	0.56

captured also by e_3. It might be that parameter g_1 also includes some modelling error due to the stiffness of non-load-bearing building elements not included in the model.

6. Inclusion of foundation in the model

In the above presented FE models, the foundation was not considered. In this section, the initial FE model is changed to take into account the flexibility of the foundation and its interaction with the soil. By performing updating of the initial model improved in this way, the effect of the foundation on the dynamic response of the building will be checked. The foundation of the Yoker building consists of several parts. Beneath the reinforced concrete ground floor slab with a thickness of 175 mm, there is a system of short reinforced concrete walls with a height of 850 mm and a thickness of 215 mm (140 mm on the edges), see Figure 17. The walls are connected at their bottom to the reinforced concrete horizontal frame with the square cross-section of 600 mm × 600 mm. Underneath the frame, there are 135 reinforced concrete piles with a diameter of 250 mm and a length of approximately 9 m.

6.1. Foundation modelling

The ground floor slab and the walls below are modelled with shell finite elements and the horizontal frame with beam finite elements. The data for the reinforced concrete are: density $\rho = 2300$ kg m^{-3}, modulus of elasticity $E = 32$ MPa and Poisson's ratio $\nu = 0.18$. The effects of the pile and the pile-soil interaction were accounted for by three orthogonal springs located at the point where the pile is attached to the horizontal frame. The stiffnesses of the horizontal and vertical spring are denoted as k_h and k_v, respectively. Moreover, the interaction between the foundation wall system (and frame) and the soil is accounted for by the horizontal area spring with stiffness k_d. The foundation part of the FE model is illustrated in Figure 17.

Stiffness values for the springs are very uncertain, but estimates can be made based on the geometrical and material properties of the piles and estimated elastic modulus of the soil (e.g. Stewart et al., 2012). The elastic modulus of the soil was estimated from twelve quick undrained triaxial compression tests at various locations under the building, which yielded values ranging from 0.9 MPa to 21.1 MPa with an average of 6.1 MPa. Using these values in the equations from a technical report by Stewart et al. (2012) gives from 1.9×10^3 N mm^{-1} to 2.3×10^4 N mm^{-1} for k_h and from 7.9×10^3 N mm^{-1} to 1.4×10^5 N mm^{-1} for k_v. Another estimate for the vertical stiffness of the pile is obtained by simply treating the pile as a bar and obtaining $k_v = \frac{E_p A_p}{L_p} = 1.67 \times 10^5$ N mm^{-1} from elastic moduli, cross-section area and pile length.

6.2. Updating of the model with foundation

The FE model updating is repeated for the initial model that takes into account the foundation. The stiffness of the springs, k_v, k_h and k_d, are added to the six parameters from Table 5. To be able to choose the range of the three newly introduced parameters and gain some further insights into these parameters, a linear (one-at-a-time) sensitivity analysis was carried out (by using the updated model from Section 5.5). For each parameter, a threshold value was found, above which the FE model behaves as if the corresponding degrees of freedom (either vertical or horizontal) are fixed, see Figure 18. This threshold is chosen to be the upper bound of the parameter range for the second model updating. The sensitivity analysis also suggests that lowering the

Table 8. Graphical comparison of initial and updated model with experimental data.

Experiments	Initial model	Updated model
$f_1 = 2.85\,\mathrm{Hz}$ 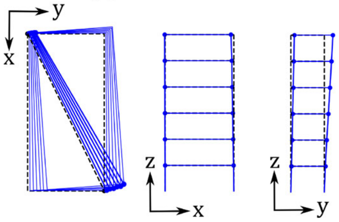	$f_1 = 2.85\,\mathrm{Hz},\ MAC_1 = 0.77$ 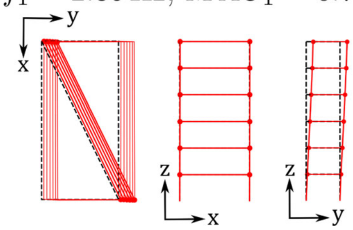	$f_1 = 2.84\,\mathrm{Hz},\ MAC_1 = 0.83$ 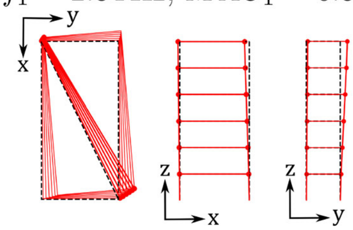
$f_2 = 2.93\,\mathrm{Hz}$ 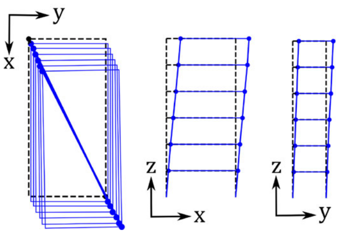	$f_2 = 2.81\,\mathrm{Hz},\ MAC_2 = 0.77$ 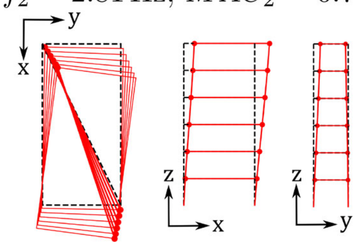	$f_2 = 2.95\,\mathrm{Hz},\ MAC_2 = 0.99$ 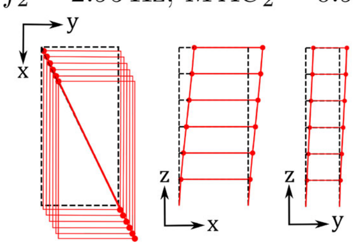
$f_3 = 3.13\,\mathrm{Hz}$ 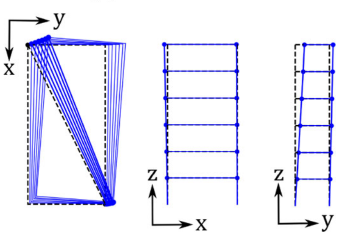	$f_3 = 2.94\,\mathrm{Hz},\ MAC_3 = 0.38$ 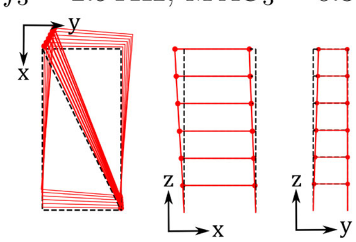	$f_3 = 3.08\,\mathrm{Hz},\ MAC_3 = 0.97$ 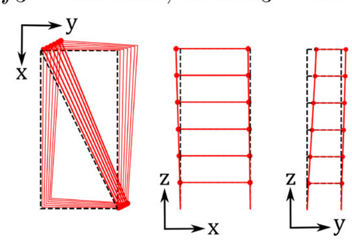
$f_4 = 3.63\,\mathrm{Hz}$ 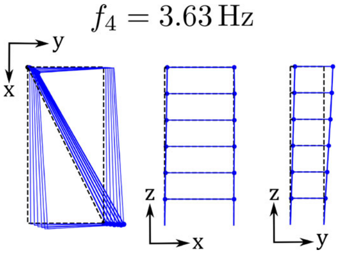	$f_4 = 3.98\,\mathrm{Hz},\ MAC_4 = 0.95$ 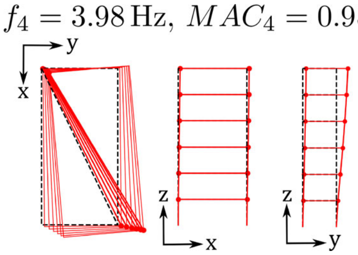	$f_4 = 3.77\,\mathrm{Hz},\ MAC_4 = 0.96$ 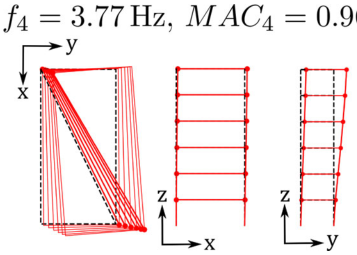
$f_5 = 6.73\,\mathrm{Hz}$ 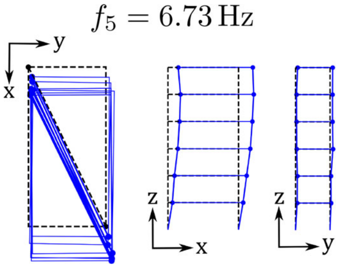	$f_5 = 8.32\,\mathrm{Hz},\ MAC_5 = 0.80$ 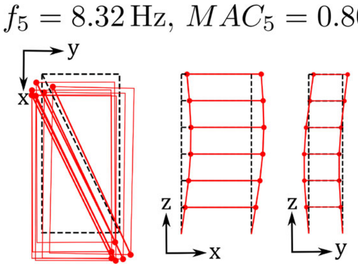	$f_5 = 6.70\,\mathrm{Hz},\ MAC_5 = 0.95$ 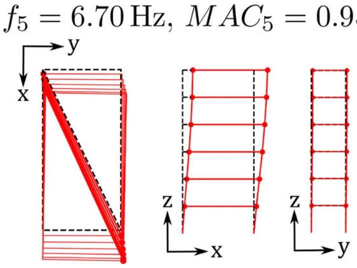
$f_6 = 8.74\,\mathrm{Hz}$ 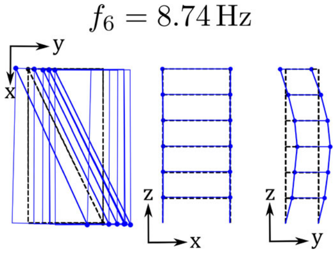	$f_6 = 8.19\,\mathrm{Hz},\ MAC_6 = 0.78$ 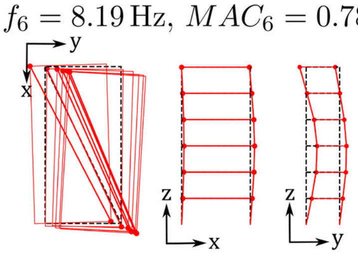	$f_6 = 8.64\,\mathrm{Hz},\ MAC_6 = 0.90$ 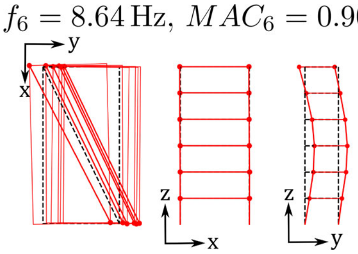

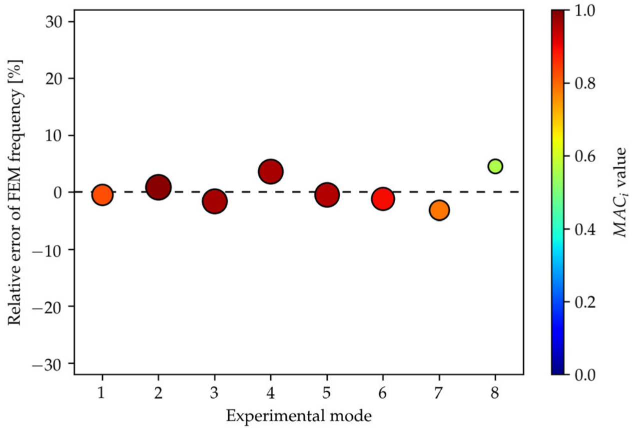

Figure 15. FMAC plot of the updated model.

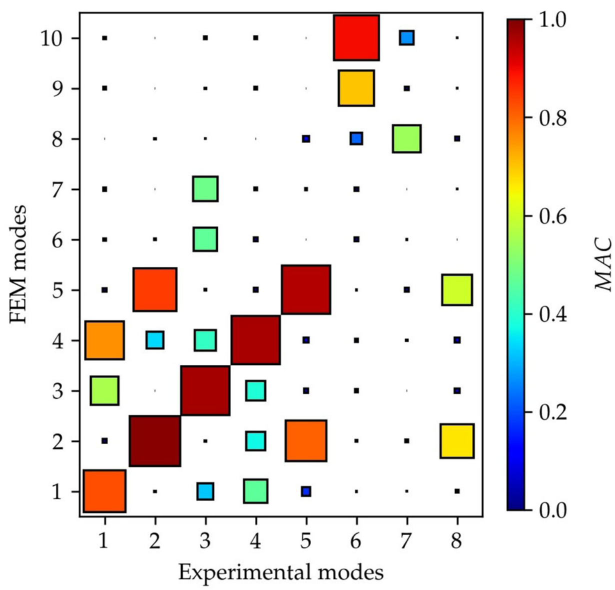

Figure 16. MAC matrix of updated model.

stiffness of parameters k_h and k_d worsens the results obtained by the first updating from Section 5.5, while the value of parameter k_v below the threshold slightly improves the mode shapes obtained by that updating.

The ranges for the three new parameters are given in Table 9. For the remaining six parameters from Table 5 the ranges did not change, except for the uncertain mass q, the range of which is now from -50 to $100\,\mathrm{kg\ m^{-2}}$. A negative value for parameter q would mean a reduction in the estimated initial mass of the building, which would also compensate for the variance in the timber density and the discrepancy of the weight of non-structural elements from the documented values.

As in the model updating in Section 5.5, a multi-objective genetic algorithm was selected for the optimization in Ansys. Due to longer computation times, the number of samples per iteration was 75 with the limit of 12 iterations. The maximum allowable Pareto percentage was 70%, and the convergence stability percentage was 1%. Objective functions from Equations (7) and (8) remain the same as for the first updating. The algorithm converged in 9 iterations with 1.33% Pareto percentage and 0.65% stability percentage

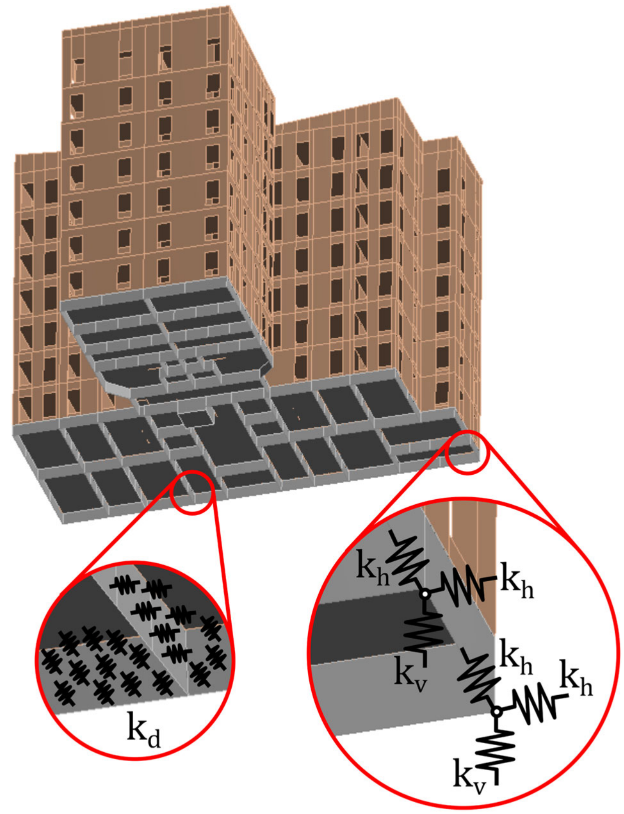

Figure 17. Modelling of the foundation.

giving three candidate points shown in Table 6. CP1 is selected as it gives the lowest δ_{freq}, see Table 10.

6.3. Results of the second updating

The resulting values of the old parameters are close to those from the first model updating (compare CP1 in Tables 6 and 10). There is a change for e_1, where the previously updated result (50.9%) changed to 59.8% of the initial value, which is still a reasonable solution according to the discussion in Section 5.6. Differences in other stiffness parameters are either not very significant (within 5% from the first updating for parameters e_3, g_1 and g_2) or they are around the mean value of the material parameter (5.2% less than the initial value for e_2). It can be concluded that for the parameter values for e_1, e_2, e_3, g_1 and g_2 from Table 10, the observations made in Section 5.6 still hold and that the values from the second updating are reasonable. The uncertain mass parameter q settles at a value of $-2.95\,\mathrm{kg\ m^{-2}}$, which, in effect, reduces the estimated initial mass of the building by 6.22%. Compared to the result of the first updating, the second updating suggests that the total mass of the building (without ground floor slab and foundation) is 91% of the total mass resulting from the first updating. This is still within the reasonable bounds for the timber building, having in mind that even the mean value for the C24 spruce density varies by more than 10% between relevant documents, see Table 2.

The newly introduced parameters provide insight into how the foundation might behave under small amplitude and low frequency range dynamic excitations. The two horizontal spring stiffness parameters (k_h and k_d) settled on

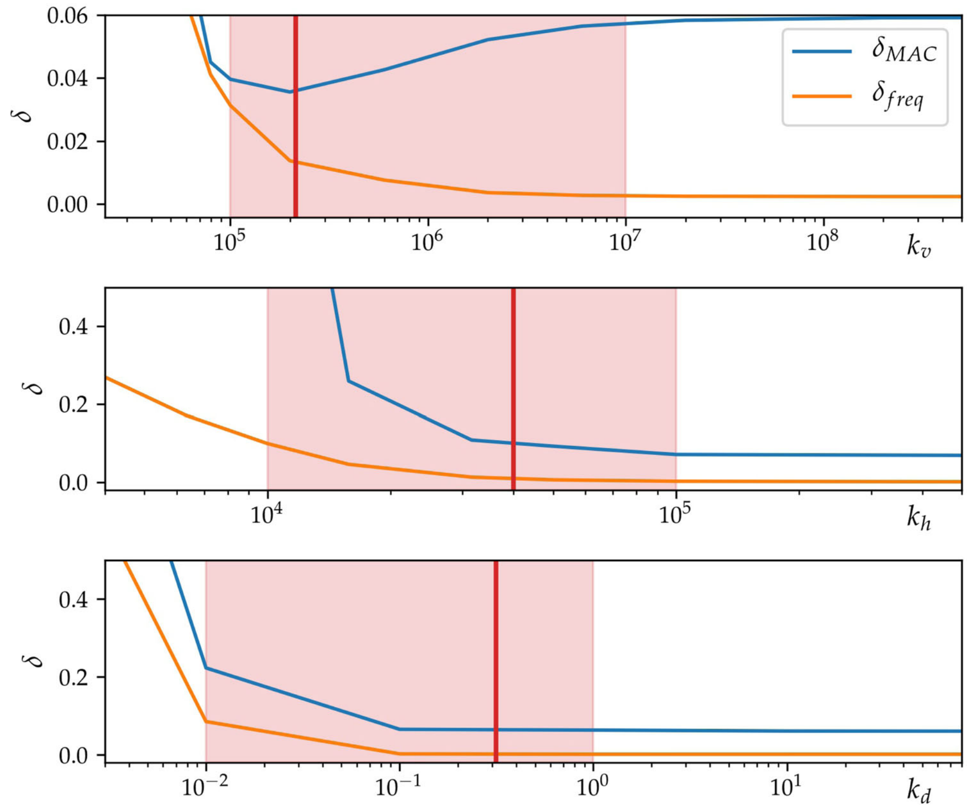

Figure 18. One-at-a-time sensitivity analysis for the spring stiffness parameters. Parameter range for the second model updating is shaded in red. The updated value is presented with red line.

Table 9. Additional parameters for the second model updating.

Parameter	Range	Description
k_h	10^4 to 10^5 N mm^{-1}	Stiffness of the horizontal springs on the locations of piles.
k_v	10^5 to 10^7 N mm^{-1}	Stiffness of the vertical springs on the locations of piles.
k_d	10^{-2} to 1 N mm^{-3}	Horizontal area spring stiffness on the foundation walls.

Table 10. Values of parameters and objective functions of the initial model and of three candidate points representing the solution of the second model updating.

Parameter	Initial model	CP1		CP2		CP3	
		Value	% of initial	Value	% of initial	Value	% of initial
e_1 [GPa]	12	7.17	59.8%	8.52	71.0%	7.16	59.7%
e_2 [GPa]	12	11.38	94.8%	10.87	90.6%	10.34	86.2%
e_3 [GPa]	12	8.42	70.2%	6.76	56.3%	7.77	64.8%
g_1 [MPa]	460	726.1	157.8%	741.5	161.2%	704.8	153.2%
g_2 [MPa]	460	213.0	46.3%	210.7	45.8%	213.0	46.3%
q [kg m^{-2}]	25	−2.95	−6.22%[1]	−6.95	−7.11%[1]	−2.61	−6.15%[1]
k_v [N mm^{-1}]		2.14e5		1.52e5		2.16e5	
k_h [N mm^{-1}]		4.00e4		6.87e4		3.88e4	
k_d [N mm^{-3}]		0.315		0.191		0.317	
δ_{freq} [$\times 10^{-3}$]	74.9	4.09		4.83		5.36	
δ_{MAC} [$\times 10^{-2}$]	58.1	4.72		4.65		4.83	

[1]Difference from initial model presented as a percentage of estimated initial mass of the building.

values near the upper bound, where the horizontal motion is almost completely restrained. Thus, the second FE model updating suggests that the horizontal motions of the foundation system are negligible. In contrast, vertical spring stiffness parameter k_v settles to a value that allows some movement according to the sensitivity analysis in Figure 18. The remaining results of the second updating, i.e. the natural frequencies and MAC values, are presented in Figures 19 and 20. They are compared with the results of the first updating in Table 11. For this comparison see also MAC matrices from Figures 16 and 19 and FMAC plots from Figures 15 and 20. The results show that by adding foundations to the FE model, matching with the experiments has not improved. In the terms of the mode shapes, there is slightly better matching with the first, but worse matching

Table 11. Comparison of results of two model updatings.

Experiments	1st updating			2nd updating		
	Frequency	Deviation	MAC_i	Frequency	Deviation	MAC_i
2.85 Hz	2.84 Hz	−0.41%	0.83	2.79 Hz	−2.11%	0.88
2.93 Hz	2.95 Hz	0.72%	0.99	2.88 Hz	−1.71%	0.99
3.13 Hz	3.08 Hz	−1.54%	0.97	3.02 Hz	−3.51%	0.96
3.63 Hz	3.77 Hz	3.75%	0.96	3.79 Hz	4.41%	0.96
6.73 Hz	6.70 Hz	−0.46%	0.95	6.80 Hz	1.04%	0.95
8.74 Hz	8.64 Hz	−1.16%	0.90	8.70 Hz	−0.46%	0.84
9.68 Hz	9.38 Hz	−3.11%	0.78	9.68 Hz	0.07%	0.73
11.9 Hz	12.4 Hz	4.30%	0.56	12.8 Hz	7.67%	0.66
δ_{freq} [$\times 10^{-3}$]		1.87			4.09	
δ_{MAC} [$\times 10^{-2}$]		4.53			4.72	

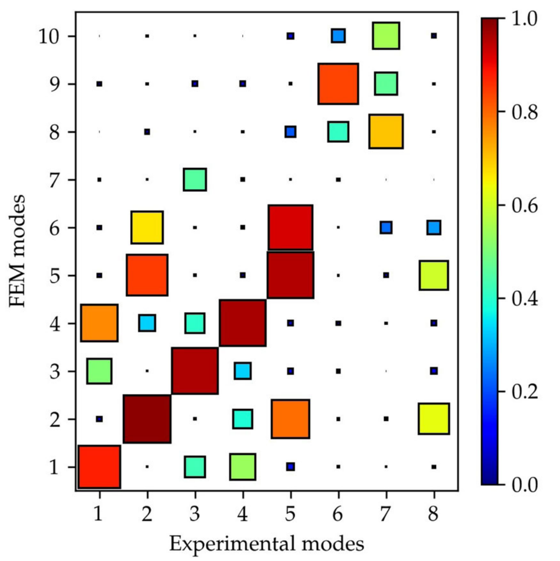

Figure 19. MAC matrix of the 2nd updated model.

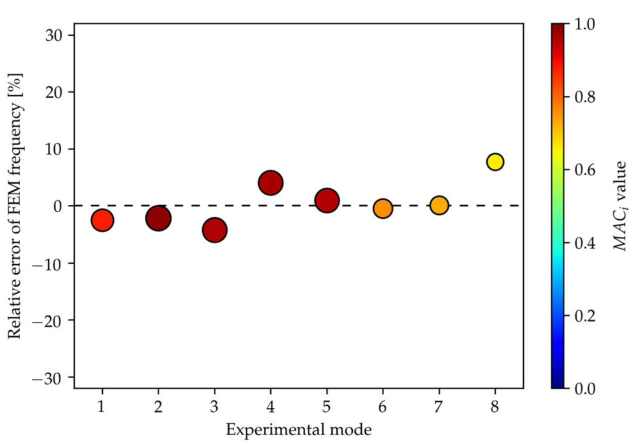

Figure 20. FMAC plot of the 2nd updated model.

with the sixth mode shape. Matching of the natural frequencies has not improved either. However, the overall results of the second updating for frequencies and MAC values are only slightly worse than those obtained in the first updating. It can be therefore concluded from the above results that for low frequency range (2 Hz to 10 Hz) and for small amplitude dynamic response (below 0.005 m/s^2), modelling of foundation is not necessary for the Yoker building.

7. Conclusions

The finite element modelling and the finite element model updating of seven-storey CLT building have been presented. The model updating was based on a successful modal testing of a building in operation that resulted in high-quality FRFs and good quality of modal estimates of the fundamental and higher modes of vibration, seldom seen in AVT-based modal testing (Ao & Pavic, 2021). Before performing the modal testing, the best-engineering-judgement FE model (called the initial FE model) of the building was prepared. Comparison of its results with the experimental leads to the following conclusion. A FE model that does not take into account the connections can predict the basic bending and torsion natural frequencies of the considered CLT building within a reasonable error (below 7%) under the conditions that:

1. A fine mesh of layered shell FEs is used to model the load-bearing components of the building (discretization error is ≈2% in our case).
2. The percentage of the non-load bearing partition walls that are not included in the model is small (≈6% in our case).
3. The dead mass of the building is carefully estimated from the design documents.
4. The uncertain mass is estimated reasonably (≈ 25 kg/m^2 in our case).
5. The mean values for the material parameters are used (in our case given by CLT manufacturer).
6. The floors are modelled as deformable.

Although not checked, it appears from the sensitivity analysis that the assumption that the CLT floors behave like rigid diaphragms might not considerably increase the error for the lowest natural frequencies. This is in line with research by Aloisio et al. (2020) where they concluded that the CLT floors behave like rigid diaphragms for the fundamental modes. Let us note, however, that the shear walls of the studied building are composed storey-wise of large CLT panels with pre-cut openings, and that any other arrangement with smaller CLT panels would very likely increase the error.

The basis for the FE model updating were the results of the input-output FRF-based modal testing, where both the excitation force and the corresponding dynamic response are measured. The performed FE model updating gave an excellent match between the results of the updated model and the experimental ones for the first six vibration modes. Based on the FE model updating, the following was found:

1. The greatest influence on the computed vibration modes has the in-plane shear stiffness of the shear walls, which is considerably higher than the estimate based on the mean in-plane shear modulus for CLT specified by the manufacturer. However, because of

large documented variance in this particular material moduli, it is difficult to state how much of the increase can be attributed to the material parameter and how much to other uncertainties.
2. The CLT floors of the considered building have large in-plane flexibility, mainly for the in-plane shearing but also for the in-plane stretching. This can be attributed to the floor connections and also to the specific floor plan of the building. Large in-plane flexibility of the CLT floors is reflected mainly for the higher modes. Our results thus show that the application of the rigid-diaphragm assumption for the CLT floors is not justified for the higher modes, but it is acceptable for the fundamental modes (as already mentioned above).
3. The wall-floor joints influence the vertical in-plane stiffness of the shear walls, which is reflected mainly for the lowest modes.
4. Inclusion of the foundation in the FE model is not necessary for small amplitudes and studied dynamic response of the observed building.

Finally, let us mention that the presented study is part of the research campaign for getting reliable data for modelling wind-induced vibrations of TTBs (see Abrahamsenet al., 2020). The idea is to estimate the key dynamic parameters of a set of existing TTBs in operation by combining modal testing and FE model updating, and make an assessment of results to generalize the findings.

Acknowledgements

The support of ERA-NET Cofund Forest Value and the corresponding funding bodies (Ministry of Education, Science and Sport of the Republic of Slovenia for BK and BB, and Forestry Commission GB for WKA) is gratefully acknowledged (DynaTTB project). BK and BB also acknowledge the financial support of the Slovenian Research Agency (J2-2490). We thank F. Perez, the designer of the Yoker building, from Smith and Wallwork Ltd at Cambridge, UK, for helpful discussions, and prof. B. Pulko from University of Ljubljana for suggestions regarding foundation modelling.

Disclosure statement

No potential conflict of interest was reported by the authors.

Funding

ERA-NET Forest Value; Ministrstvo za Izobraževanje, Znanost in Šport Republike Slovenije.

ORCID

Blaž Kurent http://orcid.org/0000-0002-9066-6433

References

Abrahamsen, R., Bjertnæs, M. A., Bouillot, J., Brank, B., Cabaton, L., Crocetti, R., … Tulebekova, S. (2020). *Dynamic response of tall timber buildings under service load – The DynaTTB research program*. Eurodyn 2020 Conference *(online)*.

Allemang, R. (2003). The modal assurance criterion – Twenty years of use and abuse. *Sound and Vibration*, *37*(8), 14–21.

Aloisio, A., Pasca, D., Tomasi, R., & Fragiacomo, M. (2020). Dynamic identification and model updating of an eight-storey CLT building. *Engineering Structures*, *413*, 110593.

Ansys®. (2020). *Ansys Academic Research Mechanical* (Release 2020 R1).

Ao, W. K., & Pavic, A. (2020). *FRF-based modal testing of sway modes using OCXO synchronised accelerometers for simultaneous force and response measurements*. Eurodyn 2020 Conference *(online)*.

Ao, W. K., & Pavic, A. (2021). *Novel wirelessly synchronised modal testing of operational buildings using distributed OCXO high-precision data loggers*. IMAC XXXIX Conference *(online)*.

Ashtari, S., Haukaas, T., & Lam, F. (2014). *In-plane stiffness of cross-laminated timber floors*. WCTE 2014 Conference.

Borgonovo, E., & Plischke, E. (2016). Sensitivity analysis: A review of recent advances. *European Journal of Operational Research*, *248*(3), 869–887. doi:10.1016/j.ejor.2015.06.032

Brandner, R., Dietsch, P., Dröscher, J., Schulte-Wrede, M., Kreuzinger, H., & Sieder, M. (2017). Cross laminated timber (CLT) diaphragms under shear: Test configuration, properties and design. *Construction and Building Materials*, *147*, 312–327. doi:10.1016/j.conbuildmat.2017.04.153

Brandner, R., Flatscher, G., Ringhofer, A., Schickhofer, G., & Thiel, A. (2016). Cross laminated timber (CLT): Overview and development. *European Journal of Wood and Wood Products*, *74*, 331–351.

Brank, B., & Carrera, E. (2000). Multilayered shell finite element with interlaminar continuous shear stresses: A refinement of the Reissner–Mindlin formulation. *International Journal for Numerical Methods in Engineering*, *48*(6), 843–874. doi:10.1002/(SICI)1097-0207(20000630)48:6<843::AID-NME903>3.0.CO;2-E

D'Arenzo, G., Casagrande, D., Reynolds, T., & Fossetti, M. (2019). In-plane elastic flexibility of cross laminated timber floor diaphragms. *Construction and Building Materials*, *209*, 709–724. doi:10.1016/j.conbuildmat.2019.03.060

Edskär, I., & Lidelöw, H. (2017). Wind–induced vibrations in timber buildings–parameter study of cross–laminated timber residential structures. *Structural Engineering International*, *27*(2), 205–216. doi:10.2749/101686617X14881932435619

Ewins, D. J. (2000). Model validation: correlation for updating. *Sadhana - Sadhana*, *25*(3), 221–234. doi:10.1007/BF02703541

Fotsch, D., & Ewins, D. (2000). Application of MAC in the frequency domain. Proceedings of the International Modal Analysis Conference - IMAC, Vol. 1, pp. 1225–1231.

Fotsch, D., & Ewins, D. (2001). *Further applications of the FMAC*. Proceedings of the International Modal Analysis Conference - IMAC, Vol. 1, pp. 635–639.

Gavric, I., Fragiacomo, M., & Ceccotti, A. (2015). Cyclic behavior of CLT wall systems: Experimental tests and analytical prediction models. *Journal of Structural Engineering*, *141*(11), 04015034. doi:10.1061/(ASCE)ST.1943-541X.0001246

Herman, J., & Usher, W. (2017). SALib: An open-source python library for sensitivity analysis. *The Journal of Open Source Software*, *2*(9), 97. doi:10.21105/joss.00097

Johansson, M., et al. (2016). *Tall timber buildings – A preliminary study of wind-induced vibrations of a 22-storey building*. WCTE 2016 - Word Conference on Timber Engineering.

Liu, K., Yan, R. J., & Guedes Soares, C. (2018). Optimal sensor placement and assessment for modal identification. *Ocean Engineering*, *165*, 209–220. doi:10.1016/j.oceaneng.2018.07.034

Malo, K. A., Abrahamsen, R. B., & Bjertnaes, M. A. (2016). Some structural design issues of the 14-storey timber framed building Treet in Norway. *European Journal of Wood and Wood Products*, *74*(3), 407–424. doi:10.1007/s00107-016-1022-5

Mottershead, J. E., Link, M., & Friswell, M. I. (2011). The sensitivity method in finite element model updating: A tutorial. *Mechanical Systems and Signal Processing*, *25*(7), 2275–2296. doi:10.1016/j.ymssp.2010.10.012

Mugabo, I., Barbosa, A. R., & Riggio, M. (2019). Dynamic characterization and vibration analysis of a four-story mass timber building. *Frontiers in Built Environment*, *5*, 86. doi:10.3389/fbuil.2019.00086

Nairn, J. A. (2017). Cross laminated timber properties including effects of non-glued edges and additional cracks. *European Journal of Wood and Wood Products*, *75*(6), 973–983. doi:10.1007/s00107-017-1202-y

Oh, J. K., Hong, J. P., Kim, C. K., Pang, S. J., Lee, S. J., & Lee, J. J. (2017). Shear behavior of cross-laminated timber wall consisting of small panels. *Journal of Wood Science*, *63*(1), 45–55. doi:10.1007/s10086-016-1591-2

Petersen, Ø. W., & Øiseth, O. (2017). Sensitivity-based finite element model updating of a pontoon bridge. *Engineering Structures*, *150*, 573–584. doi:10.1016/j.engstruct.2017.07.025

Reynolds, T., Casagrande, D., & Tomasi, R. (2016). Comparison of multi–storey cross–laminated timber and timber frame buildings by in situ modal analysis. *Construction and Building Materials*, *102*, 1009–1017. doi:10.1016/j.conbuildmat.2015.09.056

Reynolds, T., Harris, R., Chang, W.-S., Bregulla, J., & Bawcombe, J. (2015). Ambient vibration tests of a cross-laminated timber building. *Proceedings of the Institution of Civil Engineers - Construction Materials*, *168*(3), 121–131. doi:10.1680/coma.14.00047

Rocco Lahr, F. A., Christoforo, A. L., Chahud, E., Branco, L. A. M. N., Battistelle, R. A., & Valarelli, I. D. (2015). Poisson's ratios for wood species for structural purposes. *Advanced Materials Research*, *1088*, 690–693. doi:10.4028/www.scientific.net/AMR.1088.690

Saltelli, A., Ratto, M., Andres, T., Campolongo, F., Cariboni, J., & Gatelli, D. (2008). *Global sensitivity analysis. The primer*. West Sussex, UK: John Wiley & Sons, Ltd.

Shahnewaz, M., Tannert, T., Alam, M. S., & Popovski, M. (2017). In-plane stiffness of cross-laminated timber panels with openings. *Structural Engineering International*, *27*(2), 217–223. doi:10.2749/101686617X14881932436131

Stewart, J., Crouse, J. C., Hutchinson, T. C., Lizundia, B., Naeim, F., & Ostadan, F. (2012, 9). *Soil-structure interaction for building structures* [Tech. Rep. No. 12-917-21]. Gaithersburg, US: National Institute of Standards and Technology.

Stora Enso. (2019). *European Technical Assesment ETA-14/0349 of 03.06.2019* [Tech. Rep.]. Austrian Institute of Construction Engineering.

Stürzenbecher, R., Hofstetter, K., & Eberhardsteiner, J. (2010). *Cross laminated timber: A multi-layer, shear compliant plate and its mechanical behavior*. 11th World Conference on Timber Engineering 2010, WCTE 2010, Vol. 1, pp. 423–432.

Yaghoubi, V., Abrahamsson, T. (2014). The modal observability correlation as a modal correlation metric. In Allemang R., De Clerck J., Niezrecki C., Wicks A. (Eds.), *Topics in modal analysis* (Vol. 7, pp. 487–494). New York, NY: Springer.

Yasumura, M., Kobayashi, K., Okabe, M., Miyake, T., & Matsumoto, K. (2016). Full-scale tests and numerical analysis of low-rise CLT structures under lateral loading. *Journal of Structural Engineering*, *142*(4), 1–12. doi:10.1061/(ASCE)ST.1943-541X.0001348